Computational analysis of current-loss mechanisms in a post-hole convolute driven by magnetically insulated transmission lines

D. V. Rose,* E. A. Madrid, D. R. Welch, R. E. Clark, and C. B. Mostrom
Voss Scientific, LLC, Albuquerque, New Mexico 87108, USA

W. A. Stygar and M. E. Cuneo
Sandia National Laboratories, Albuquerque, New Mexico 87185, USA
(Received 29 August 2014; published 4 March 2015)

Numerical simulations of a vacuum post-hole convolute driven by magnetically insulated vacuum transmission lines (MITLs) are used to study current losses due to charged particle emission from the MITL-convolute-system electrodes. This work builds on the results of a previous study [E. A. Madrid *et al.* Phys. Rev. ST Accel. Beams 16, 120401 (2013)] and adds realistic power pulses, Ohmic heating of anode surfaces, and a model for the formation and evolution of cathode plasmas. The simulations suggest that modestly larger anode-cathode gaps in the MITLs upstream of the convolute result in significantly less current loss. In addition, longer pulse durations lead to somewhat greater current loss due to cathode-plasma expansion. These results can be applied to the design of future MITL-convolute systems for high-current pulsed-power systems.

DOI: 10.1103/PhysRevSTAB.18.030402 PACS numbers: 84.70.+p, 52.58.Lq, 52.65.Rr

I. INTRODUCTION

One approach to combining the current in multiple vacuum transmission lines and delivering the combined current to a single line is to employ a vacuum post-hole convolute. The single transmission line then drives a load. This approach is used on a number of high-power machines such as the Saturn [1,2] and Z [3] (see Ref. [4] for a list of relevant publications) accelerators in the United States, the Primary Test Stand [5,6] in China, and the Angara-5-1 [7], MIG [8] and Baikal [9] generators in Russia. In the absence of charged particle emission and plasma formation along the vacuum facing surfaces, this technique is very efficient. At high power levels, charged particle emission and electrode plasma formation result in portions of the current being lost and therefore not available to drive the load. Understanding the nature of these losses can lead to improvements in the performance of current and future higher-current accelerators [10,11].

In a previous paper [4], the scaling of these losses was explored under the assumption of quasiequilibrium operation using 3D particle-in-cell (PIC) simulations. In Ref. [4], the upstream magnetically insulated transmission lines (MITLs), post-hole convolute, and final vacuum transmission line were modeled as a *coupled* system. Electron sheath current launched from the cathode surfaces in the transmission lines upstream of the convolute was found to flow along Poynting vector (i.e., $\vec{E} \times \vec{B}$) streamlines [4]. It was also found that the magnitude of the sheath current flowing into the convolute largely determined the current loss.

The simulation model presented in Ref. [4] is expanded in the present work to include (i) a time-dependent electrical-power-pulse, (ii) a self-consistent model for Ohmic heating of the anode surfaces, and (iii) a cathode-plasma-formation model [12]. Using this expanded simulation model, some of the geometric design variations explored in Ref. [4] are revisited and the scaling of current loss under a variety of particle emission model combinations is studied. The main objective of this work is to obtain an understanding of current loss due to different charged-particle formation models, leading to improved design criteria. When a simulation includes space-charge-limited (SCL) emission from cathodes and ion emission from the anodes, but not cathode-plasma formation and expansion, the quasiequilibrium model results of Ref. [4] are in good agreement with the time-dependent results presented here. When a simulation also includes the formation and expansion of cathode plasma (which are not studied in Ref. [4]), higher loss current magnitudes are obtained which are driven primarily by increased electron sheath currents entering the convolute.

The exact nature of current losses in the vacuum section of the Z machine are not well known and detailed measurements are challenging [13,14]. For example, loss currents between 1 and 4 MA have been observed on Z for relatively low-impedance loads [15]. Several models for these losses have been developed (see, for example, the discussion in Ref. [4]).

*David.Rose@vosssci.com

The numerical simulations presented in this work are somewhat idealized, yet qualitatively representative of the upper levels of the Z MITL-convolute system; physical dimensions, time scales, and field amplitudes are consistent with Z. As such, the model in this form is not well suited to the detailed analysis of specific Z shots. (For examples of numerical simulations of specific Z shots, see Refs. [12,16–20].) The model presented here does enable the study of the complex interaction between magnetically insulated sheath currents generated upstream of the convolute with the post-hole convolute. These simulations examine the scaling of current losses in the presence of different charged particle sources as described above. To further simplify the analysis, all simulations use a fixed load impedance, rather than a time-dependent load impedance model, such as those used to model specific shots [12].

This paper is organized as follows. In Sec. II, the simulation model is described and the key differences between the present model and that used in Ref. [4] are highlighted. In Sec. III, a series of *baseline* simulation results are described. Where applicable, direct comparison to the results obtained in Ref. [4] are given. In Sec. IV, the results of a number of simulations incorporating various parameter changes are described. These variations include driver and load characteristics, geometric changes to the transmission line and convolute dimensions, and plasma model parameter scans. A summary is given in Sec. V along with a brief discussion of the possible implications for convolute and transmission line system design and operation.

II. SIMULATION MODEL

The PIC code Lsp [21] is used to conduct fully kinetic, fully electromagnetic (EM), relativistic, 3D cylindrical (r, θ, z) simulations to examine current losses in a coupled MITL-convolute system. A variable time step $\Delta(t)$ is programmed to resolve both the electron-cyclotron (ω_{ce}) and electron-plasma (ω_{pe}) frequencies such that $[\omega_{ce}(t), \omega_{pe}(t)]\Delta(t) < 2$. Cell sizes throughout the simulation volume are fixed at 1 mm in the r direction and vary between 0.25 mm to 1 mm in the z direction. The smallest cell sizes in the z direction correspond to the cathode faces in the A and B MITLs [see Fig. 1(a)]. The azimuthal cell size is fixed at 0.0131 radians.

This simulation model is similar to that described in Ref. [4], with some minor differences including the removal of a step in the lower anode, the addition of a longer final coaxial MITL (connected to the load), and a somewhat larger outer radius for the A and B MITLs. The anode step provides a more accurate representation of the Z convolute hardware, but was found in Ref. [4] to have no significant effect on the current loss and therefore was eliminated. The additional coaxial transmission line between the final radial transmission line and the load improves numerical stability in these longer time-duration runs by symmetrizing EM wave and particle flows exiting the system through this wave-transmitting boundary. Finally, the larger outer radius for the A and B radial MITLs in the new simulations tends to give a larger sheath current entering the convolute. This change was intended to improve understanding of where large-amplitude, thick electron flows [22] would be lost in the convolute region.

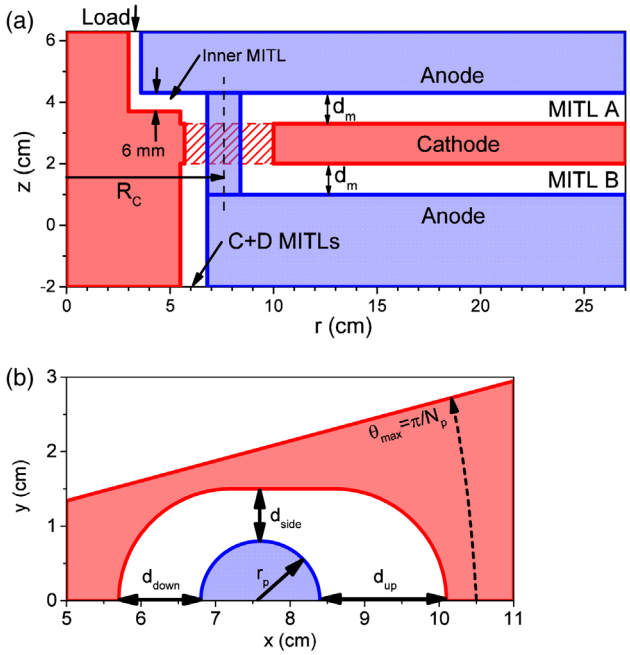

FIG. 1. Schematics of the simulation geometry. In (a) the simulation setup is shown in the $\theta = 0$ plane that bisects the anode post, and in (b) a cross section of the cathode hole and anode post are shown. Key design parameter variables are indicated.

The simulation geometry is illustrated in Fig. 1 and explicitly treats the upper two MITLs and upper half of an idealized double post-hole convolute system, reducing the computational time required to complete a simulation [4]. The lower two MITLs and post-hole convolute are removed and the corresponding electromagnetic powers are combined and coupled to the upper convolute via a coaxial feed. Hence current losses occurring in the two lower radial MITLs and convolute are not modeled.

The key physical dimensions are based on the Z accelerator. The simulations use symmetry boundaries between $0 \le \theta \le \theta_{\max}$, where $\theta_{\max} = \pi/N_p$, and N_p is the number of posts in the upper convolute (joining MITLs A and B). The simulation region extends in radius between 3 cm and 27 cm. The A and B MITL gap spacings (d_m) are constant, with $d_m = 1$ cm as the baseline value. The cathode plate separating the two MITL levels is 1.3 cm thick. The hole in the cathode plate approximates the shape of the upper cathode hole in the Z convolute. The baseline anode post radius (r_p) is 0.8 cm. The radial position of the convolute is characterized by R_c, the distance between the machine axis and the center of the anode post.

Power is delivered into the simulation through three wave transmitting boundaries: a coaxial port at $z = -2$ cm represents the combined power delivered from the lower C and D MITLs; and two ports at $r = 27$ cm deliver power into MITLs A and B. Downstream of the convolute, power is delivered to the load along a single radial transmission line with a 6 mm anode-cathode (AK) gap that transitions to a coaxial transmission line. A final wave transmitting boundary at $z = 6.3$ cm is coupled to a simple circuit model that sets the load impedance, Z_{Load}.

A relatively large, time-independent load impedance is used. Large impedance values provide high electric fields early in the pulse that initiate electron emission. Thus significant sheath currents develop which in turn result in relatively large loss current values over a wide range of operating parameters, allowing differentiation between different design points.

We note that the circuit model connecting the final coaxial transmission line to the load enables time-dependent load models to be used for analysis of specific shots (see, for example, Refs. [12,16,23]). Dynamic load models, for example wire-arrays, produce load impedances that vary in time, generating backward-traveling waves that modify the electron sheath properties, and therefore the loss currents. Such an analysis is beyond the scope of this study.

For all simulations, linearly rising voltage waveforms are injected through the three wave transmitting boundaries. In the absence of any charged particle emission, this gives a linearly rising current at the load with dI/dt equal to a constant over a pulse length τ_p. After $t = \tau_p$, the injected waveform is set to give a constant power for roughly 30 ns in order to collect quasiequilibrium values for the various quantities of interest [4].

Electrons are emitted from cathode surfaces using a relativistically correct SCL model [24] with an electric field threshold of 240 kV/cm. This emission threshold is consistent with several published estimates for stainless steel and aluminum cathode materials (see, for example, Ref. [25]).

Electron energy deposition and Ohmic current conduction (see below) rapidly heat anode surfaces, leading to dense surface plasma formation. Ions are subsequently accelerated from these thin, high-density anode plasmas. The model assumes SCL emission of ions (H^+) directly from surfaces for which the local temperature has increased by 400 K. This threshold condition for anode ion emission is based on experimental evidence from high-power, charged-particle diode experiments (see, for example, Refs. [26,27]).

The cathode plasma formation model [12] assumes the explosive emission of electrons and desorption of a neutral, thermal particle layer from a conducting surface at a prescribed rate. Plasma desorption is initiated on a cell-by-cell basis once the local electric field exceeds the threshold set for SCL electron emission. The neutral desorption rate, D, of 7.5×10^{-3} ml/ns [1 monolayer $(\mathrm{ml}) = 10^{15}\,\mathrm{cm}^{-2}$] is the baseline value used here since it was found to give reasonable agreement with measured loss currents in previous 3D convolute simulations [12,20]. This value of D lies within typical ranges of contaminant desorption rates in pulsed-power vacuum operating environments [28].

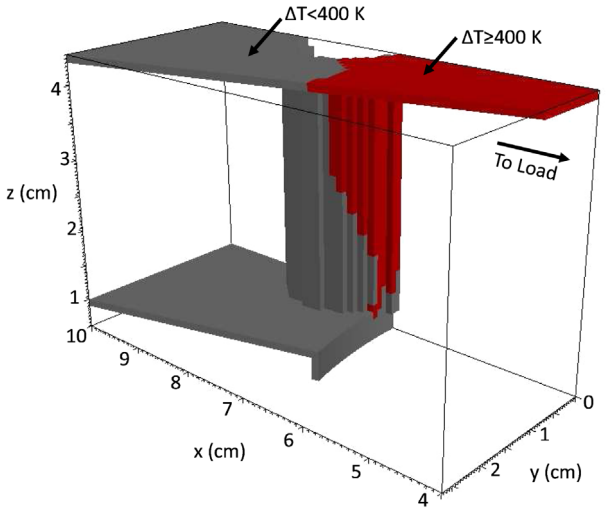

FIG. 2. Surface temperature increase along anode components due to Ohmic heating from a $dI/dt = 0.2$ MA/ns pulse after 100 ns. The gray shaded regions do not reach $\Delta T = 400$ K for this calculation.

The simulations include a model for Ohmic or resistive heating of anode surfaces due to time-dependent surface currents. For a linearly rising, lineal current density $j(t)$ (current per unit length), the surface temperature increase as a function of time can be expressed as [29]

$$\Delta T(t) \simeq \frac{1.273\mu_0 j^2(t)}{2c_v}, \tag{1}$$

in SI units, where c_v is the specific heat of the electrode material at constant volume (stainless steel with $c_v = 3 \times 10^6$ J/m^3 K is assumed) and where the coefficient 1.273 is obtained from Table 10.IV of Ref. [29]. (Previously Schumer *et al.* [23] used a similar calculation to predetermine trigger times for anode ion emission in simulations of a high-current conical transmission line.)

To illustrate the impact of Ohmic heating on the anode surface temperature, Fig. 2 plots the anode surfaces with $\Delta T \geq 400$ K (red shaded regions) at $t = \tau_p = 100$ ns for operating voltage $V_0 = 6$ MV and total anode current $I_A = 20$ MA ($dI/dt = 0.2$ MA/ns). This result is from a "cold test" simulation, i.e., one that does not include any charged particle emission. Therefore it is reasonable to expect that the entire final MITL and most of the downstream side of the anode post emit ions by the end of the power pulse.

III. BASELINE SIMULATION RESULTS

The baseline simulation geometry is shown in Fig. 1 with key numerical parameters summarized in Table I. To establish nominal operating conditions, baseline geometry simulations were carried out for three combinations of particle emission models: (i) SCL electron emission (e) from cathode surfaces, (ii) SCL electron emission from cathode surfaces and SCL ion emission from anode surfaces (e/i), and (iii) SCL electron emission, SCL ion emission, and cathode plasma emission (e/i/p).

Currents as a function of time for each of these cases are plotted in Fig. 3. The total anode current, I_A, is obtained by summing the anode currents at large radius in MITLs A and B with the anode current flowing in the coax representing the contribution from MITLs C and D. The load current, I_{Load}, is measured in the circuit element representing the fixed impedance load. The loss current is then $I_{\mathrm{Loss}} = I_A - I_{\mathrm{Load}}$. The electron emission case, Fig. 3(a), gives a relatively small current loss (< 1 MA) throughout the pulse. At early times, $0 < t \lesssim 35$ ns, the loss current is highest, prior to the onset of magnetic insulation of the electron sheath in the MITLs. The electron and ion emission case, Fig. 3(b), gives a loss current that rises linearly between $40 \lesssim t \lesssim 100$ ns. Adding cathode plasma emission, shown in Fig. 3(c), significantly increases the loss current. The dynamics of this loss mechanism are addressed below and in Sec. IV.

Characterization of the quasiequilibrium operating conditions are obtained by averaging the electrical measurements between times $\tau_p + 5$ ns and $\tau_p + 30$ ns and are listed in Table II. The loss current fraction, listed in the last column of this table, is defined as

$$f_\ell = \frac{I_A - I_{\mathrm{Load}}}{I_A} = \frac{I_{\mathrm{Loss}}}{I_A}. \tag{2}$$

TABLE I. Summary of key simulation parameters and baseline values.

Variable	Description	Baseline Value
τ_p	Pulse duration	100 ns
dI/dt	Current rise rate	0.2 MA/ns
V_0	Voltage at $t \geq \tau_p$	6.0 MV
Z_{Load}	Load impedance (constant)	0.3 Ω
N_p	Number of posts	12
d_m	MITL AK gap spacing	1.0 cm
R_c	Convolute radial position	7.6 cm
r_p	Post radius	0.8 cm
d_{up}	Upstream convolute AK gap	1.7 cm
d_{down}	Downstream convolute AK gap	1.1 cm
d_{side}	Azimuthal convolute AK gap	0.7 cm
D	Plasma desorption rate	7.5×10^{-3} ml/ns
r^e_{max}	Max. radius for particle emission	25 cm

This variable is used extensively in this work as a quality parameter for comparison between the simulation results.

A. Cathode electron emission

For run 2* with only cathode electron emission enabled, $f_\ell \simeq 4\%$, consistent with Ref. [4]. The total sheath current, I_s, listed in Table II, is the sum of the sheath current flowing in the A and B MITLs measured 1 cm upstream of the cathode hole. For run 2*, $I_s = 0.7$ MA, roughly equal to the loss current. Thus as observed previously [4], essentially all of the sheath current launched in the MITLs upstream of the convolute is lost to the anode structures.

As discussed in detail in Ref. [4], the sheath current obtained in these simulations is larger than 1D models predict. One estimate of the equilibrium sheath current in a constant impedance MITL is [16,30,31]

$$I_s \simeq \frac{V^2}{2 I_A^m Z_v^2} = 2\pi^2 \frac{\epsilon_0}{\mu_0} \frac{V^2 r^2}{I_A^m d_m^2}, \tag{3}$$

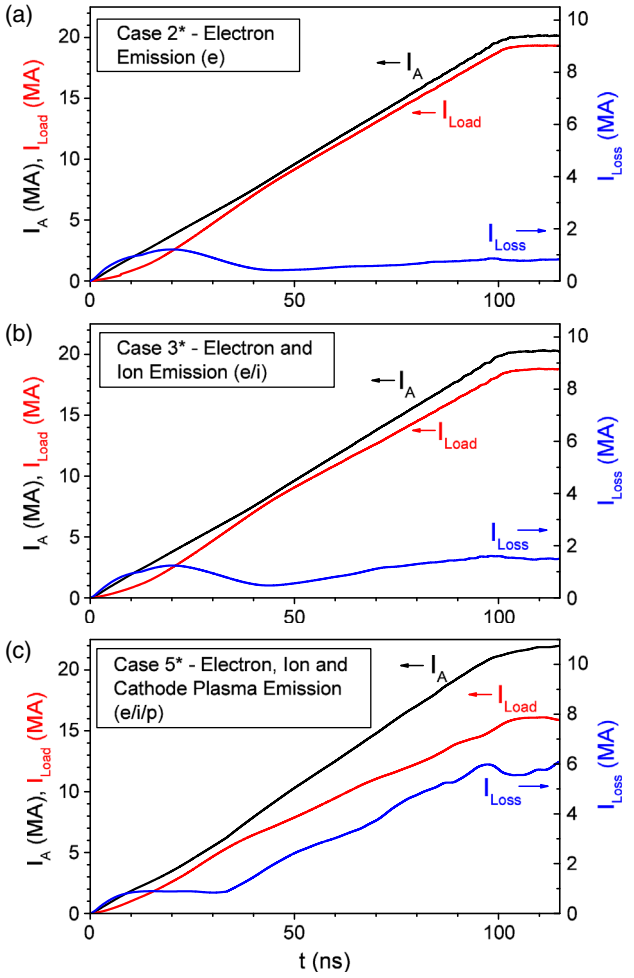

FIG. 3. Upstream anode current (I_A), load current (I_{Load}), and loss current $I_{\mathrm{Loss}} = I_A - I_{\mathrm{Load}}$ for the three baseline cases; (a) 2*, (b) 3*, and (c) 5*.

TABLE II. Summary of simulation results. The run labels with a "*" are baseline cases described in Sec. III. The letter "r" appended to a run label indicates the selected emission model has been restricted to a radius less than or equal to the stated value ($r^e_{\max}$). The emission model labels are defined as follows; "e" refers to SCL electron emission from cathode surface locations with $|E| \geq 240$ kV/cm, "i" refers to ion (H^+) emission from anode surfaces that undergo a temperature increase of $\Delta T \geq 400$ K, and "p" refers to cathode plasma emission (H^+-electron) at a constant desorption rate D once local SCL electron emission commences.

Run Label	Emission Models	Description	V_0 (MV)	I_A (MA)	I_{Load} (MA)	I_{Loss} (MA)	I_s (MA)	f_ℓ
1	None	Cold Test Vacuum Case	6.0	20.00	20.00	0.0	0.0	0%
2*	e	Baseline electron emission for all cathode surfaces	5.8	20.13	19.32	0.81	0.7	4%
2r	e	- Restrict emission, $r^e_{\max} = 10.2$ cm	6.0	20.00	19.77	0.23	0.0	1%
3*	e/i	Baseline electron/ion emission	5.7	20.29	18.77	1.52	0.7	7%
3r	e/i	- Restrict emission, $r^e_{\max} = 10.2$ cm	5.8	20.14	19.30	0.84	0.0	4%
4	e/p	Add cathode plasma formation to run 2*	5.0	20.90	16.77	4.13	3.5	20%
4r	e/p	- Restrict emission, $r^e_{\max} = 10.2$ cm	5.9	20.07	19.53	0.54	0.0	3%
5*	e/i/p	Baseline electron/ion/plasma emission	4.6	21.29	15.45	5.84	3.3	27%
5r	e/i/p	- Restrict emission, $r^e_{\max} = 10.2$ cm	5.7	20.09	19.00	1.09	0.0	5%
5i	e/i/p	- Plasma desorption rate, $D = 2.5 \times 10^{-3}$ ml/ns	5.4	20.53	17.91	2.62	1.3	13%
5ii	e/i/p	- Plasma desorption rate, $D = 5.0 \times 10^{-3}$ ml/ns	4.9	21.02	16.27	4.75	2.7	23%
5iii	e/i/p	- Plasma desorption rate, $D = 1.0 \times 10^{-2}$ ml/ns	4.6	21.38	15.09	6.29	3.3	29%
6	e/i	50% drive voltage	2.8	10.12	9.46	0.66	0.2	7%
7	e/i/p	50% drive voltage	2.4	10.52	8.11	2.41	1.7	23%
8	e/i	50% load impedance ($Z_{\text{Load}} = 0.15\ \Omega$)	3.3	22.54	22.15	0.39	0.2	2%
9	e/i/p	50% load impedance ($Z_{\text{Load}} = 0.15\ \Omega$)	2.9	22.88	19.87	3.01	1.8	13%
10	e/i	Longer rise time ($\tau_p = 200$ ns)	5.6	20.31	18.73	1.57	0.7	8%
11	e/i/p	Longer rise time ($\tau_p = 200$ ns)	4.5	21.45	14.90	6.55	3.1	31%
11r	e/i/p	- Restrict emission, $r^e_{\max} = 10.2$ cm	5.7	20.23	18.98	1.25	0.0	6%
12	e/i	Larger MITL AK gaps ($d_m = 1.4$ cm)	5.8	20.28	19.18	1.10	0.3	5%
13	e/i/p	Larger MITL AK gaps ($d_m = 1.4$ cm)	5.0	20.87	16.49	4.38	2.5	21%
13r	e/i/p	- Restrict emission, $r^e_{\max} = 10.2$ cm	5.8	20.27	19.26	1.01	0.0	5%
13i	e/i/p	- Plasma desorption rate, $D = 2.5 \times 10^{-3}$ ml/ns	5.4	20.53	18.04	2.49	1.2	12%
13ii	e/i/p	- Plasma desorption rate, $D = 5.0 \times 10^{-3}$ ml/ns	5.0	20.81	16.70	4.11	2.3	20%
13iii	e/i/p	- Plasma desorption rate, $D = 1.0 \times 10^{-2}$ ml/ns	5.0	20.85	16.60	4.25	2.7	20%
14	e/i	50% anode post radius ($r_p = 0.4$ cm)	5.6	20.28	18.80	1.48	0.7	7%
15	e/i/p	50% anode post radius ($r_p = 0.4$ cm)	4.5	21.35	15.07	6.28	3.2	29%
15r	e/i/p	- Restrict emission, $r^e_{\max} = 10.2$ cm	5.7	20.19	19.12	1.07	0.0	5%
16	e/i	Fewer anode posts ($N_p = 10$)	5.6	20.29	18.76	1.53	0.7	8%
17	e/i/p	Fewer anode posts ($N_p = 10$)	4.8	21.14	15.84	5.30	3.2	25%
17r	e/i/p	- Restrict emission, $r^e_{\max} = 10.2$ cm	5.7	20.19	19.12	1.07	0.0	5%
18	e/i	Increase gaps in convolute ($R_c = 8.1$ cm)[a]	5.7	20.55	19.12	1.43	0.7	7%
19	e/i/p	Increase gaps in convolute ($R_c = 8.1$ cm)[a]	4.6	21.68	15.19	6.49	3.2	30%
19r	e/i/p	- Restrict emission, $r^e_{\max} = 10.2$ cm	5.8	20.50	19.34	1.16	0.0	6%

[a]With $r_p = 0.3$ cm, $r_{\text{up}} = 2.6$ cm, $r_{\text{down}} = 1.6$ cm, $r_{\text{side}} = 1.5$ cm.

where Z_v is the MITL vacuum impedance and I^m_A is the anode current in the MITL (SI units). Another example, given in Ref. [22], that includes collisional effects in the MTIL is

$$I_s \simeq \frac{9V^2}{8I^m_A Z^2_v}. \tag{4}$$

For example, the sheath current flowing in the A MITL in run 2* is roughly 0.35 MA. Assuming values of $r = 15$ cm, $d_m = 1$ cm, $V = 5.8$ MV, and $I^m_A = 5.03$ MA ($I^m_A \simeq I_A/4$), Eq. (3) gives a sheath current of roughly 0.21 MA, and Eq. (4) gives 0.47 MA. These analytic values bound those obtained in the simulation. The sheath thickness in these simulations is much greater than typical 1D theoretical estimates, as discussed in Ref. [4]. This is largely due to the spatial resolution, which is insufficient to resolve the sheath.

Eliminating the sheath current flowing from the MITLs results in a loss current fraction of 1%. These losses are due to electron emission in the convolute itself and final radial MITL. This result is shown in Table II, run 2r, where no

charged particle emission is enabled for $r > r^e_{\max} = 10.2$ cm. This result sets a lower limit on the current loss fraction expected in any simulation that includes charged particle emission.

B. Cathode electron and anode ion emission

For the baseline cathode-electron and anode-ion emission run (3*), a current loss fraction of 7% is obtained. This value is in good agreement with the previous result of Ref. [4]. For a more direct comparison to loss current estimates from previous convolute simulations that do not include electron sheath flow from long (>2 cm) MITL sections [12,20], run 3r was carried out with $r^e_{\max} = 10.2$ cm. This reduces the loss current fraction from 7% to 4%. This is still much larger than typical loss currents obtained in Refs. [12,20], although direct comparison is complicated by the differences in the load models used in these two cases.

C. Cathode electron, anode ion, and cathode plasma emission

The baseline electron, ion, and cathode plasma emission run (5*) gives a significantly larger total loss current fraction, 27%, for $D = 7.5 \times 10^{-3}$ ml/ns. Previous simulation studies using this plasma desorption rate resulted in loss current fractions that were largely consistent with measured current losses on Z [12,20]. Our present simulation model is significantly different in several ways relative to the previous results; (i) the simulations of Refs. [12,20] used a time-dependent model for the load dynamics which gives a significantly lower impedance (and therefore a lower voltage) throughout the rising current pulse, (ii) the previous simulations used ~2-cm-long MITL sections upstream of the convolute rather than the ~15-cm-long sections used here, (iii) the previous simulations limited the cathode surfaces over which plasma formation was enabled to the vicinity of the cathode holes, (iv) the previous simulations constrained anode ion emission to the posts, and finally (v) the previous simulations did not include a model for Ohmic heating of the anode surfaces. We find that the highly nonuniform electron sheaths tend to enhance the acceleration of plasma formed at cathode surfaces out into the gaps of the long MITLs. This, in turn, leads to smaller *effective* MITL gaps and larger sheath currents. For this run, roughly four times the electron sheath current is launched in the MITLs upstream of the convolute relative to the electron-emission-only case (2*).

As noted above, previous simulations [12,20] did not include a model for Ohmic heating (described in Sec. II). Disabling the Ohmic heating model, so that electron energy deposition is the sole source of anode surface heating, was tested by repeating run 5r. A loss current fraction of 2% (not included in Table II) was obtained. Therefore the simulation results in Refs. [12,20] likely underestimated the total surface areas and time scales over which anode ion emission was active.

Previous simulations with very short length transmission lines upstream of the convolute showed that the main source of current loss resulted from a collection of plasma on the downstream side of the post [12,20]. Plasma flows from the cathode upstream of the collection location along magnetic field lines and accumulates on the downstream side of the post. The gradually increasing density of the plasma in this region results in the formation of a small *effective* gap between the cathode plasma and the anode post. Complex electron drifts in the crossed electric and magnetic fields in this small gap result in electrons crossing from the collected plasma to the anode.

In the present simulations, plasma also collects on the downstream side of the post. This is illustrated in Fig. 4 which plots plasma ion iso-density contours and magnetic field streamlines at $t = 60$ ns from run 5r. The magnetic field streamlines shown in this figure flow from the upper gap and downward in z into the convolute on the downstream side of the post. Plasma created along the cathode

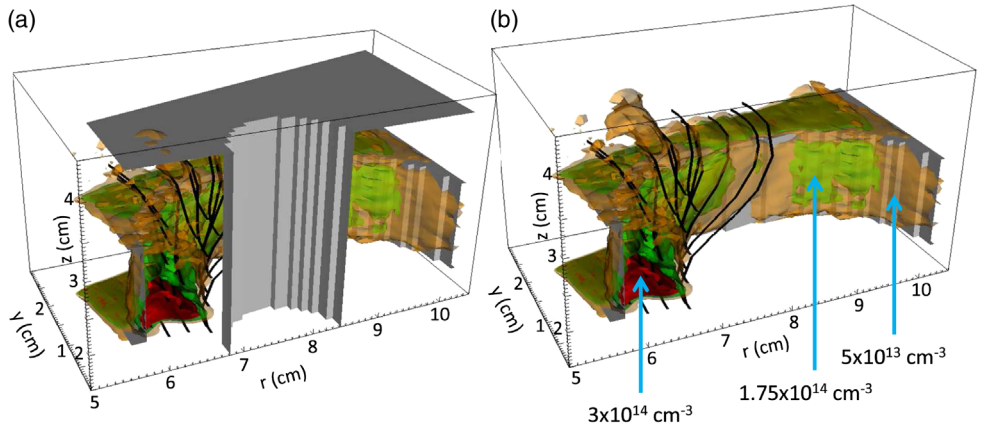

FIG. 4. (a) Plasma iso-density contours and magnetic field streamlines at $t = 60$ ns from run 5r. In (b), the anode components of the convolute are removed from the image.

surface can then flow along these streamlines and collect on the downstream side of the post. As the plasma density on the downstream side of the post reaches a critical value (roughly greater than 10^{14} cm^{-3}), the plasma layer becomes an effective extension of the cathode, and can then be a SCL electron source. The small effective plasma-to-post gap results in large electric fields that can accelerate electrons from the plasma layer as well as ions from the anode post. The presence of plasma on the downstream side of the post has been inferred from spectroscopic measurements [14].

Comparison of runs 5* and 5r indicates that this particular current loss mechanism is not the dominant one for simulations that include cathode plasma in the upstream MITLs. Rather, the cathode plasma in these transmission lines leads to substantially increased electron sheath currents; comparing runs 2* and 5* shows a factor of 4 increase in the sheath current entering the convolute from the MITLs. The magnitude of the sheath current is a function of the plasma desorption rate and is discussed in Sec. IV.

Run 5r was repeated with the Ohmic heating model disabled. This case (not listed in Table II) results in a reduction in f_ℓ from 5% to 4%. This change is consistent with the results discussed above.

IV. PARAMETER STUDIES

A. Operating parameter variations

Runs 6 through 11 in Table II briefly explore changes to the electrical operation of the convolute system. Runs 6 and 7 use a 50% reduction in the drive voltage. In the limit of only cathode electron emission, Ref. [4] demonstrated that the current loss fraction changes very slowly with drive voltage. Here, comparing run 6 with run 3*, the loss current fraction is unchanged, as expected. Adding cathode plasma emission, the loss current fraction increases measurably from run 7 (23%) to run 5* (27%).

We find that the cathode plasma expansion rate increases with voltage, decreasing the effective MITL gap, and increasing the sheath current in the MITLs. This observation is consistent with other simulation results that model electrode plasma formation [32–37]. Here the underlying mechanism is associated with the highly nonuniform sheath current that occurs in the variable impedance MITLs; electron vortices at the edge of the plasma layer generate electric field reversals that pull plasma ions out into the MITL gap. In addition, highly resolved 2D MITL simulations have shown development of an instability at the electrode-plasma/electron-sheath boundary, leading to enhanced cross-field diffusion [36,37].

Runs 8 and 9 revisit the impact of the load impedance on the loss current fraction discussed in detail in Ref. [4]. That work showed that in the limit of cathode electron emission, the load current scales roughly as Z_{Load}^2 [16,22,30,31]. In the limit of cathode electron and anode ion emission, runs 8 (2%) and 3* (7%) encompass a factor of two increase in Z_{Load} resulting in f_ℓ scaling consistent with Ref. [4]. Comparing the loss current fractions of the cathode plasma runs 9 (13%) and 5* (27%), a more modest scaling of f_ℓ with Z_{Load} is suggested.

Examination of current loss scaling under the constraints of this model is considered in runs 10 and 11 where τ_p is increased to 200 ns, reducing dI/dt to 0.1 MA/ns. In the limit of cathode electron and anode ion emission, the loss current fraction increases only slightly with increased pulse duration, while the addition of cathode plasma emission increases the loss current fraction from 27% (run 5*) to 31% (run 11). This increase in f_ℓ is consistent with increased current loss in the convolute through the plasma fill mechanism described in Sec. III C. Evidence for this is obtained from run 11r, which gives a slightly larger (6%) value of f_ℓ relative to run 5r (5%). In this case, the increased current loss is associated with the additional time that the cathode plasma has to fill the vacuum gap on the downstream side of the post.

B. Geometric variations

In the absence of cathode plasma formation, the sheath current magnitude as a function of physical MITL gap, d_m, follows the expected $1/d^2$ scaling as predicted by Eqs. (3) and (4) (see, for example, runs 3* and 12). In the runs including cathode plasma formation in the MITLs, the net electron sheath current is carried partly inside and partly outside of the plasma layer. The presence of the dynamic electron sheath drives a nonuniform thickness plasma layer along the cathode in the MITLs. The layer thickness generally increases with decreasing radius in all cases, and the plasma density is not uniform in the r or z directions. Averaging spatially between $0 \le \theta \le \pi/12$ and $15 < r < 19$ cm, an estimate of the plasma density profile across the MITL A gap can be obtained. The plasma layer has a roughly exponentially decreasing density profile.

This is illustrated in Fig. 5 for different values of D in simulations with $d_m = 1.0$ and 1.4 cm. The spatial axis is normalized as $(z - z_k)/d_m$ where z_k is the position of the MITL A cathode. It is expected that the effective plasma layer thickness will reach a maximum for some value of D. This is the case in Fig. 5(b) where the ion density profiles for $D = 7.5 \times 10^{-3}$ and 1.0×10^{-2} ml/ns are roughly equal. In Fig. 5(a), the convergence to a maximum plasma layer is not obtained for $D \ge 7.5 \times 10^{-3}$ ml/ns due to sheath current being lost to the anode along the A MITL which does not happen in the $d_m = 1.4$ cm case shown in Fig. 5(b). The black points shown in Fig. 5 indicate the approximate position at which the electric field effectively goes to zero within the denser plasma (within the limit of signal noise), forming the "edge" of the effective cathode.

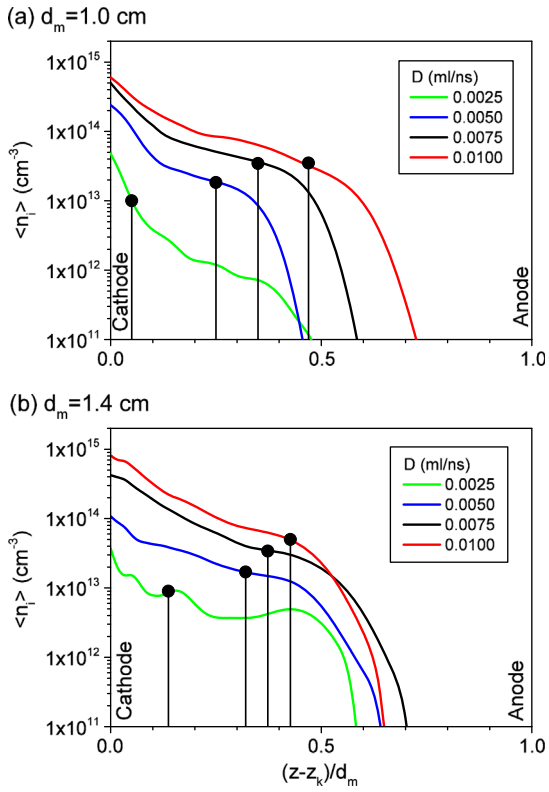

FIG. 5. Spatially averaged ion density profiles in the A MITL for (a) $d_m = 1$ cm and (b) $d_m = 1.4$ cm. The approximate effective cathode position in the gap for each case is indicated by the black point.

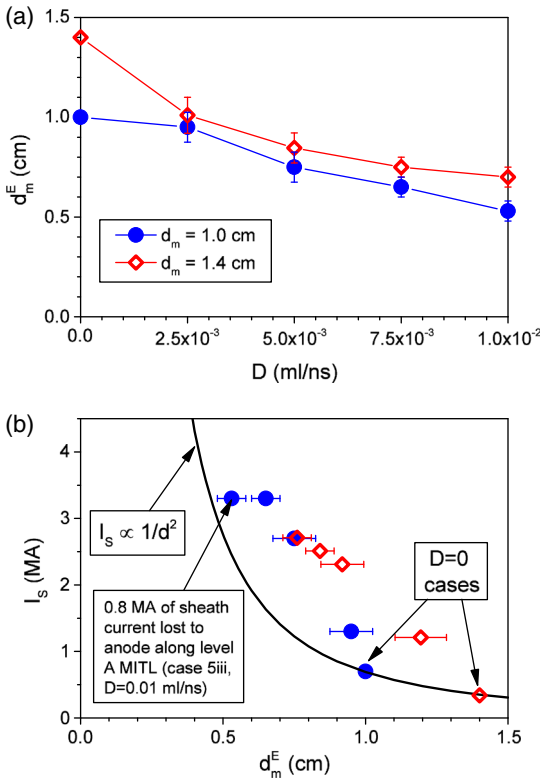

FIG. 6. (a) Estimated effective AK gap (d_m^E) from simulations with different plasma desorption rates, D. (b) Scaling of the simulated sheath current in the MITLs upstream of the convolute as a function of d_m^E.

The effective AK gap width in the MITLs was estimated from spatially averaged radial current density profiles for times after quasiequilibrium operation. ($t > \tau_p$). The net radial current density as a function of z (and the E_z field profile) was used to estimate the position within the gap at which significant radial current flow was established. This position was deemed the effective cathode location from which the effective AK gap, d_m^E, was then determined. Values of d_m^E are plotted as a function of D for two values of d_m in Fig. 6(a). The error bars of the individual data points are rough estimates of the uncertainty in the analysis. For $D = 0$, $d_m^E \equiv d_m$; and for increasing values of D, the effective AK gap decreases.

Plotting the sheath current from Table II as a function of the estimated effective AK gap in Fig. 6(b) illustrates the scaling of the sheath current as a function of the effective AK gap. For illustration purposes, the solid curve gives the $1/d^2$ scaling from Eqs. (3) and (4) expected for gaps determined by solid, perfectly conducting electrodes *or* by a dense, conductive, hard-edged electrode plasma. From Fig. 5, the plasma density that evolves in these simulations is not hard-edged, and the current carrying-electron sheath lies partially within this ion density profile, modifying the resultant sheath properties.

Additional parameter variations listed in Table II examine the impact of a smaller diameter anode post (runs 14 and 15), fewer anode posts (runs 16 and 17), and a post-hole convolute that incorporates larger spacing between the face of the cathode hole and the anode post.

For the case of the smaller anode post diameter, the cathode-electron and anode-ion emission run (14) gives the same value of f_ℓ (7%) as run 3*. Code diagnostics suggest that electron current lost to the post is relatively small (< 0.1 MA) when the post diameter is reduced by 50%. (For comparison, run 3* loses roughly 0.8 MA of current to the post.) Therefore in the limit of a large electron sheath current entering the convolute (roughly 0.7 MA), electrons striking the post can be reduced, but are then lost elsewhere in the system.

Comparing the cases that include cathode plasma formation (runs 5* and 15), the loss current fraction increases slightly for the smaller post diameter. The current lost to the posts does indeed decrease for the smaller post diameter case (1.3 MA for run 5* to < 0.1 MA for run 15), but again the overall current loss in the system is similar (27% for run 5* and 29% for run 15).

Another convolute design idea explored on Z was the use of fewer anode posts to reduce current loss [20]. The idea is that fewer posts each conducting more current are better insulated against electron bombardment leading to ion emission. In Ref. [4], this topic was explored for 6, 10,

and 12 post simulations using SCL electron emission from cathode surfaces at $Z_{\mathrm{Load}} = 0.3\ \Omega$. A modest reduction in the loss current fraction was obtained when the number of posts was reduced from 12 to 6 ($f_\ell = 3.5\%$ for 12 posts and 3.0% for 6 posts).

In Table II, run 16 uses 10 posts and gives a slightly higher loss current fraction (8%) than run 3*. The current lost to the posts is slightly higher for run 16 (0.9 MA), suggesting that the additional magnetic insulation in the case of fewer posts is insufficient to change the total current striking the posts. This observation is consistent with the 10 post simulation presented in Ref. [4].

Adding cathode plasma emission to the 10 post case (run 17) results in a slightly lower loss current fraction (25%) than run 5*, and the current lost to the posts is also slightly reduced relative to run 5* (1.2 MA for run 17 versus 1.3 MA for run 5*). Run 17r indicates that plasma accumulation in the gap on the downstream side of the post is similar to the 12 post result (run 5r). These conclusions are qualitatively supported by 9-post convolute shots on Z which gave loss current magnitudes that were similar to 12-post standard convolute shots with identical loads [20].

Finally, larger gaps between the cathode hole edge and the anode post were tested. The anode post diameter was reduced from 1.6 cm to 6 mm and the cathode hole size was increased in all directions for runs 18 and 19. The hole dimensions are included in Table II. The larger cathode hole also required that the radial position of the convolute be increased from $R_c = 7.6$ cm to 8.1 cm. For cathode electron and anode ion emission (run 18), the loss current fraction was the same (7%) as the baseline case (run 3*). The current lost to the posts was < 0.1 MA, consistent with run 14, which used an 8 mm diameter post. Adding cathode plasma emission (run 19) resulted in a somewhat larger loss current fraction (30%) than the baseline run 5* (27%).

V. SUMMARY AND DISCUSSION

This work extends the previous analysis of Madrid *et al.* [4]. The simulation model allows for relatively rapid analysis of current loss processes in a time-accurate description of a coupled MITL-convolute system. In addition, the present work includes a model for Ohmic heating of anode surfaces, and a model for cathode plasma formation and dynamics.

The results presented herein are directly applicable to Sandia's refurbished Z accelerator, the PTS accelerator, the Baikal accelerator, and next-generation pulsed-power accelerators.

As in Ref. [4], most of the simulations use a fixed load impedance with a relatively large value ($Z_{\mathrm{Load}} = 0.3\ \Omega$). A large value of Z_{Load} throughout the power pulse results in electric field amplitudes that initiate electron emission early in the pulse and results in significant electron sheath currents. This, in turn, provides relatively large loss current values under a wide range of operating conditions, allowing clear differentiation between different design points.

Design insight gained from the simulations presented in this work include; (i) modestly larger MITL AK gaps give significantly smaller loss currents and (ii) longer pulse durations lead to somewhat higher loss currents due to cathode plasma expansion, as expected. In the limit of relatively large electron sheath currents entering the convolute, we again find that current flow through the magnetic field nulls is not the main source of current loss in these systems.

ACKNOWLEDGMENTS

The authors are extremely grateful for the sustained support of this research by J. L. Porter, D. G. Flicker, M. C. Herrmann, D. O. Jobe, M. L. Keifer, J. S. Lash, K. R. LeChien, M. K. Matzen, L. X. Schneider, and R. F. Schneider. We acknowledge helpful discussions with M. R. Gomez, R. B. Campbell, D. B. Reisman, C. Thoma and J. Gansz. This work is supported by the Department of Energy through Sandia National Laboratories. Sandia National Laboratories is a multi-program laboratory operated by Sandia Corporation, a wholly owned subsidiary of Lockheed Martin Company, for the U.S. Department of Energy's National Nuclear Security Administration under Contract No. DE-AC04-94AL85000.

[1] D. D. Bloomquist, R. W. Stinnett, D. H. McDaniel, J. R. Lee, A. W. Sharpe, J. A. Halbleib, L. G. Schlitt, P. W. Spence, and P. Corcoran, in *Proceedings of the 6th IEEE Internation Pulsed Power Conference, Arlington, VA, 1987*, edited by P. J. Turchi and B. H. Bernsein (IEEE, Piscataway, NJ, 1987), p. 310.

[2] R. B. Spielman, P. Corcoran, J. Fockler, H. Kishi, and P. W. Spence, in *Proceedings of the 7th IEEE International Pulsed Power Conference, Monterey, CA, 1989*, edited by B. H. Bernstein and J. P. Shannon (IEEE, Piscataway, NJ, 1989), p. 445.

[3] R. B. Spielman, W. A. Stygar, J. F. Seamen, F. Long, H. Ives, R. Garcia, T. Wagoner, K. W. Struve, M. Mostrom, I. Smith *et al.*, in *Proceedings of the 11th IEEE International Pulsed Power Conference, Baltimore, MD, 1997*, edited by G. Cooperstein and I. Vitkovitsky (IEEE, Piscataway, NJ, 1997), p. 709.

[4] E. A. Madrid, D. V. Rose, D. R. Welch, R. E. Clark, C. B. Mostrom, W. A. Stygar, M. E. Cuneo, M. R. Gomez, T. P. Hughes, T. D. Pointon *et al.*, Phys. Rev. ST Accel. Beams **16**, 120401 (2013).

[5] J. K. Dan, X. B. Huang, S. Q. Zhang, S. T. Zhou, X. D. Ren, S. C. Duan, K. Ouyang, H. C. Cai, M. Wang, S. P. Feng *et al.*, in *Proceedings of the 19th IEEE Internation Pulsed Power Conference, San Francisco, CA, 2013*, edited by B. V. Oliver, J. P. Verboncoeur, and M. T. Crawford (IEEE, Piscataway, NJ, 2013), p. 967.

[6] Z. Wenkang, G. Fan, S. Shengyi, W. Meng, X. Weiping, and D. Jianjun, Phys. Rev. ST Accel. Beams **17**, 110401 (2014).

[7] Z. A. Al'bikov, E. P. Velikov, A. I. Veretennikov, V. A. Glukhikh, E. V. Grabovskii, G. M. Gryaznov, O. A. Gusev, G. N. Zhemchuzhnikov, V. I. Zaitsev, O. A. Zolotovskii *et al.*, Sov. At. Energy **68**, 34 (1990).

[8] S. A. Sorokin, Tech. Phys. **56**, 957 (2011).

[9] E. A. Azizov, V. V. Alexander, S. G. Alikhanov, V. H. Bachtin, V. I. Chetvertkov, V. A. Glukhikh, E. V. Grabovskii, A. N. Gribov, Y. A. Hallimullin, V. A. Levashov *et al.*, in *Dense Z-Pinches: 5th International COnference on Dense Z-Pinches, AIP Conference Proceedings Vol. 651*, edited by J. Davis, C. Deeney, and N. R. Pereira (American Institute of Physics, Melville, New York, 2002), p. 29.

[10] W. A. Stygar, M. E. Cuneo, D. I. Headley, H. C. Ives, R. J. Leeper, M. G. Mazarakis, C. L. Olson, J. L. Porter, and T. C. Wagoner, Phys. Rev. ST Accel. Beams **10**, 030401 (2007).

[11] D. R. Welch, T. C. Genoni, D. V. Rose, N. Bruner, and W. A. Stygar, Phys. Rev. ST Accel. Beams **11**, 030401 (2008).

[12] D. V. Rose, D. R. Welch, T. P. Hughes, R. E. Clark, and W. A. Stygar, Phys. Rev. ST Accel. Beams **11**, 060401 (2008).

[13] W. A. Stygar, P. A. Corcoran, H. C. Ives, R. B. Spielman, J. W. Douglas, B. A. Whitney, M. A. Mostrom, T. C. Wagoner, C. S. Speas, T. L. Gilliland *et al.*, Phys. Rev. ST Accel. Beams **12**, 120401 (2009).

[14] M. R. Gomez, M. E. Cuneo, R. D. McBride, G. A. Rochau, D. J. Ampleford, J. E. Bailey, A. D. Edens, B. Jones, M. Jones, M. R. Lopez *et al.*, in *Proceedings of the 18th IEEE Internation Pulsed Power Conference, Chicago, Il, 2011*, edited by R. D. Curry and B. V. Oliver (IEEE, Piscataway, NJ, 2011), p. 688.

[15] W. A. Stygar, H. C. Ives, D. L. Fehl, M. E. Cuneo, M. G. Mazarakis, J. E. Bailey, G. R. Bennett, D. E. Bliss, G. A. Chandler, R. J. Leeper *et al.*, Phys. Rev. E **69**, 046403 (2004).

[16] T. D. Pointon, W. A. Stygar, R. B. Spielman, H. C. Ives, and K. W. Struve, Phys. Plasmas **8**, 4534 (2001).

[17] T. D. Pointon and M. E. Savage, in *Proceedings of the 15th IEEE Pulsed Power Conference, Monterey, CA, 2005*, edited by J. Manechen and E. Schamiloglu (IEEE, Piscataway, NJ, 2005), p. 151.

[18] T. D. Pointon, W. L. Langston, and M. E. Savage, in *Proceedings of the 16th IEEE Pulsed Power and Plasma Science Conf, Albuquerque, NM, 2007*, edited by E. Schamiloglu and F. Peterkin (IEEE, Piscataway, NJ, 2007), p. 165.

[19] T. D. Pointon and D. B. Seidel, in *Proceedings of the 17th IEEE International Pulsed Power Conference, Washington, DC, 2009*, edited by F. Peterkin and R. Curry (IEEE, Piscataway, NJ, 2009), p. 1159.

[20] D. V. Rose, D. R. Welch, R. E. Clark, E. A. Madrid, C. L. Miller, C. Mostrom, W. A. Stygar, M. E. Cuneo, C. A. Jennings, B. Jones *et al.*, in *Proceedings of the 17th IEEE International Pulsed Power Conference, Washington, DC, 2009*, edited by F. Peterkin and R. Curry (IEEE, Piscataway, NJ, 2009), p. 1153.

[21] D. R. Welch, D. V. Rose, M. E. Cuneo, R. B. Campbell, and T. A. Mehlhorn, Phys. Plasmas **13**, 063105 (2006).

[22] W. A. Stygar, T. C. Wagoner, H. C. Ives, P. A. Corcoran, M. E. Cuneo, J. W. Douglas, T. L. Gilliland, M. G. Mazarakis, J. J. Ramirez, J. F. Seamen *et al.*, Phys. Rev. ST Accel. Beams **9**, 090401 (2006).

[23] J. W. Schumer, P. F. Ottinger, and C. L. Olson, IEEE Trans. Plasma Sci. **34**, 2652 (2006).

[24] R. E. Clark, D. R. Welch, W. R. Zimmerman, C. L. Miller, T. C. Genoni, D. V. Rose, D. W. Price, P. N. Martin, D. J. Short, A. W. P. Jones *et al.*, J. Comput. Phys. **230**, 695 (2011).

[25] M. S. Di Capua and D. G. Pellinen, J. Appl. Phys. **50**, 3713 (1979).

[26] A. E. Blaugrund, G. Cooperstein, and S. A. Goldstein, Phys. Fluids **20**, 1185 (1977).

[27] T. W. L. Sanford, J. A. Halbleib, J. W. Poukey, A. L. Pregenzer, R. C. Pate, C. E. Heath, R. Mock, G. A. Mastin, D. C. Ghiglia, T. J. Roemer *et al.*, J. Appl. Phys. **66**, 10 (1989).

[28] M. E. Cuneo, IEEE Trans. Dielectr. Electr. Insul. **6**, 469 (1999).

[29] H. Knoepfel, *Pulsed High Magnetic Fields* (North Holland, London, 1970).

[30] C. W. Mendel, Jr., D. B. Seidel, and S. E. Rosenthal, Lasers and Particle Beams **1**, 311 (1983).

[31] T. D. Pointon and W. A. Stygar, in *Proceedings of the 13th IEEE Pulsed Power Conference, Las Vegas, NV, 2001*, edited by B. Reinovsky and M. Newton (IEEE, Piscataway, NJ, 2001), p. 1696.

[32] D. V. Rose, D. R. Welch, and T. C. Genoni, *Bull. Am. Phys. Soc.* ***52****, 243 (2007)*.

[33] D. R. Welch, D. V. Rose, N. Bruner, R. E. Clark, B. V. Oliver, K. Hahn, and M. Johnston, Phys. Plasmas **16**, 123102 (2009).

[34] D. V. Rose, C. L. Miller, S. Portillo, and D. R. Welch, Phys. Plasmas **20**, 034501 (2013).

[35] J. E. Coleman, D. C. Moir, C. A. Ekdahl, J. B. Johnson, B. T. McCuistain, and M. T. Crawford, in *Proceedings of the 41st IEEE International Conference on Plasma Science and the 20th International Conference on High-Power Particle Beams, Washington, DC, 2014, to appear*, edited by J. Schumer (IEEE, Piscataway, NJ, 2014).

[36] C. Thoma, T. C. Genoni, and D. R. Welch, in *Proceedings of the 41st IEEE International Conference on Plasma Science and the 20th International Conference on High-Power Particle Beams, Washington, DC, 2014, to appear*, edited by J. Schumer (IEEE, Piscataway, NJ, 2014).

[37] C. Thoma, T. C. Genoni, and D. R. Welch (to be published).